# Deliverable 2.9 Project report on seismic tomography data interpretation and conceptual model for integrating DAS into borehole seismic tomography surveying

## Digital monitoring of $CO_2$ storage projects


Prepared by

Uta Koedel (Geotomographie GmbH)

Thomas Fechner (Geotomographie GmbH)

Anna Stork (SILIXA)



DigiMon Deliverable D.2.9 Version 1.0,

13 September 2022

The Digimon, project no 299622 is supported by the ACT international initiative http://www.act-ccs.eu/about-us and funded by GASSNOVA (NO), RCN (NO), BEIS (UK), Forschungszentrum Jülich (DE), GSRT (GR), RVO (NL), UEFISCDI (RO), DoE (US), Repsol Norge (NO) and Equinor (NO)

## Revision

| Version | Date | Change | Page |
|---|---|---|---|
| 1.0 | 13.09.2022 | First version | All |

## Document distribution

### ACT Coordinator

- Research Council of Norway

### ACT national funding agencies

- Forschungszentrum Jülich GmbH, Projektträger Jülich, (FZJ/PtJ), Germany.
- Geniki Grammatia Erevnas kai Technologias/The General Secretariat for Research and Technology (GSRT), Greece.
- Ministry of Economic Affairs and Climate/Rijksdienst voor Ondernemend Nederland (RVO), the Netherlands.
- The Research Council of Norway (RCN), Norway.
- Gassnova, Norway.
- Development and Executive Agency for Higher Education, Research, Development and Innovation Funding (UEFISCDI), Romania.
- Department for Business, Energy and Industrial Strategy (BEIS), U.K.
- Department of Energy (DoE), USA.

### DigiMon partners

- NORCE Norwegian Research Centre AS
- OCTIO Environmental Monitoring AS
- NTNU Norwegian University of Science and Technology
- University of Bristol
- University of Oxford
- CRES Centre for Renewable Energy Sources and Saving
- Helmholtz–Centre for Environmental Research
- Sedona Development SRL
- TNO Nederlandse Organisatie voor toegepast -natuurwetenschappelijk Onderzoek
- Geotomographie GmbH
- LLC Lawrence Livermore National Security
- SILIXA LTD
- EQUINOR ASA
- REPSOL –NORGE AS

## Table of contents

# 1 Introduction Seismic Tomography and Crosswell experiments

## 1.1 Operation principle

The term tomography (from the ancient Greek τομή =" cut" and γράφειν =" to write") refers to various imaging techniques that can determine the internal spatial structure of an object and represent it in the form of sectional images (also called slice images or tomograms). Tomography covers various imaging techniques that can determine the internal spatial structure of an object and represent it in the form of sectional images (also called slice images or tomograms). Production of these images is based on the various mathematical procedure for tomographic reconstruction, such as the Simultaneous Iterative Reconstruction Technique (SIRT) in geophysics [Dines and Lytle, 1979].

In seismic tomography, the line on which the integral values are obtained is usually the (in inhomogeneous material, not straight) connecting line between seismic source and receiver (travel path). This can be determined numerically by ray-tracing methods. The used integral value (sum of values) along this line can be either the traveltime of the wave (traveltime tomography) or the attenuation (amplitude tomography). Traveltime tomography is based on ray tracing and uses only the direct arrival times. It results additively from the traveltimes in individual sections of the travel path defined by the slowness (1/v) in the corresponding path elements. In amplitude tomography, the total attenuation (amplitude decrease) results multiplicatively from the attenuations in the individual path elements. In order to arrive at an integral value (sum value), the logarithms of the amplitudes are used, whereby the multiplicative connection becomes an additive one.

Seismic tomography is a technique for imaging the subsurface of the Earth with seismic waves produced by earthquakes or explosions. Compressional wave velocities ($V_P$), shear wave velocities ($V_S$) and surface waves can be used for tomographic models of different resolutions based on seismic wavelength, wave source distance, and the seismograph array coverage. Seismic tomography provides high-resolution 2D or 3D images of the different waves between boreholes.

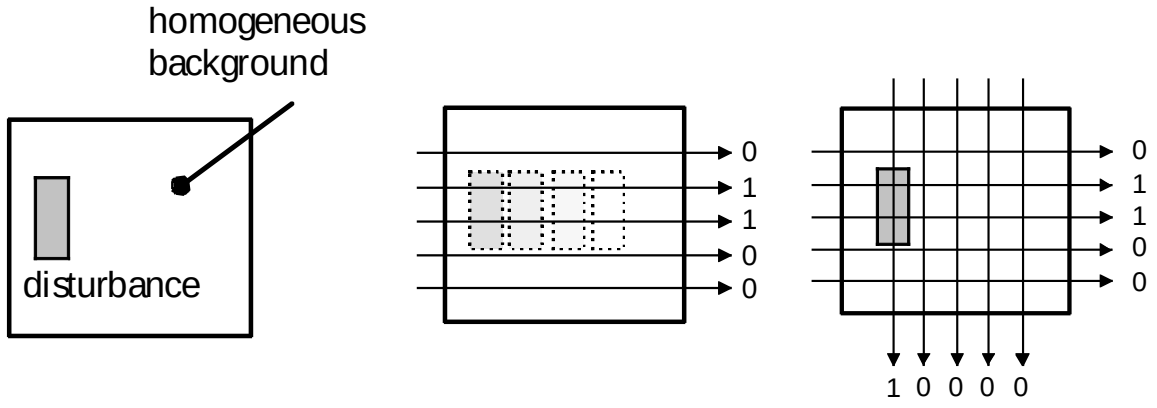


*Figure 1: Principle of seismic tomography. A high-resolution structural velocity image is calculated (an inverse problem for 1D information to a 2D or 3D image) based on traveltimes. Example indicates that if only one ray direction is available, the correct location of the disturbance can not be obtained. This is only possible if additional directions are considered.*

While Seismic tomography can be applied to different geometries can be applied in different geometries, such as crosswell or cross-hole (between two boreholes), VSP (Vertical Seismic Profiling) or surface wave, we only refer to crosswell experiments and body waves ( P-and S-waves) in this description.

Crosswell experiments take advantage of generating and recording (seismic) body waves, both the P- and S-waves, at selected depth intervals where the source and receiver(s) are maintained at equal elevations for each measurement (see Figure 2). Cross-well test provides a depth profile of shear wave velocities ($V_S$) and compressional wave velocities ($V_P$) between boreholes at a high vertical resolution.

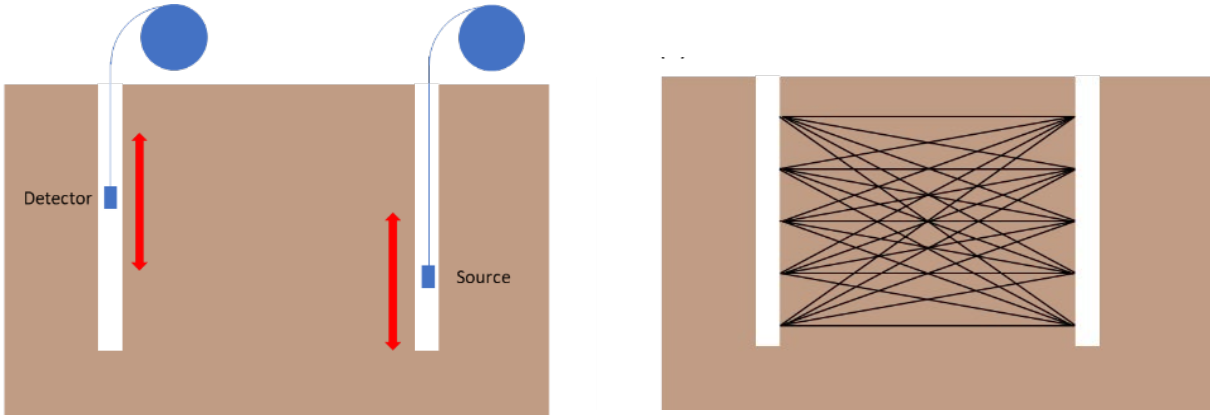


*Figure 2. Schematic setup for conventional tomographic borehole seismic experiments. Seismic ray paths defining source and detector positions for conventional borehole tomography experiments*

Crosswell seismic tomography measures the two-dimensional velocity field between two boreholes. A colour-coded map usually represents the velocity field, referred to as a tomogram, in which a colour is assigned to the seismic velocity at each point. Crosswell tomographic data is processed using algorithms that simultaneously reconstruct both the seismic velocity field in the subsurface and the path of the energy through it. Algorithms based on ray tracing or wave equations are usually used. These algorithms solve nonlinear equations to reconstruct the velocity field between the boreholes for compressional and/or shear waves.

With its at least four times higher resolution, crosswell seismic tomography offers a solution to the poor resolution in conventional seismic data [Pereira and Jone, 2010]. In most cases, P-wave tomography is used to predict high-resolution spatial continuity of lithological structures where P-waves are generated in one borehole and transmitted to the other. P-wave tomography is a common approach for subsurface characterization and has become an integrated tool routinely used for surveying development sites considered for major building projects, such as dams and building constructions. However, the groundwater table strongly influences the P-wave; therefore, its application for deriving geotechnical parameters is limited. Cosma et al. (2009) applied traveltime tomography to the time-lapse cross-well data acquired at the Ketzin Site to monitor the $CO_2$ injection. Their results indicated that conventional *P*-wave cross-well traveltime tomography could not map the $CO_2$ distribution at the time of the surveys since no significant first-arrival traveltime variations were observed. In contrast, shear waves react sensitively to changes in dynamic soil parameters, such as shear strength or modulus of elasticity. Due to the heterogeneous structure of the soil, these parameters also have a 3D structure.

The standard P-wave tomographic acquisition geometries are generally applicable for high-resolution S-wave tomography. However, S-wave tomography is employed internationally and nationally in a relatively limited number of studies predominately motivated by academic interests. P- and S-wave tomographic results of previous studies show a significantly higher velocity contrast for S-wave tomograms (factor 3) than P-wave tomograms

(factor 1.5). A joint inversion of S- and P-wave tomographic data reduces the inherent ambiguity of tomographic reconstruction techniques.

## 1.2 Processing Workflow for Tomographic Inversion

The first step of the tomographic inversion workflow is the data acquisition of crosswell data (see Figure 3). Usually, the acquisition software generates one stacked data file per depth and excitation direction in the format seg2 or segY. Then, these data files can be imported into seismic software that allows the first arrival picking, such as ReflexW. If the quality is reasonable, the picking can be done, and the picks should be adjusted manually. If the data are picked separately, it is necessary to join all picks in one data file. Some software available allows to join the several picking files and include the true borehole deviation. This software allows a validity check where picks outside a specific and adjustable velocity depth range can be removed.

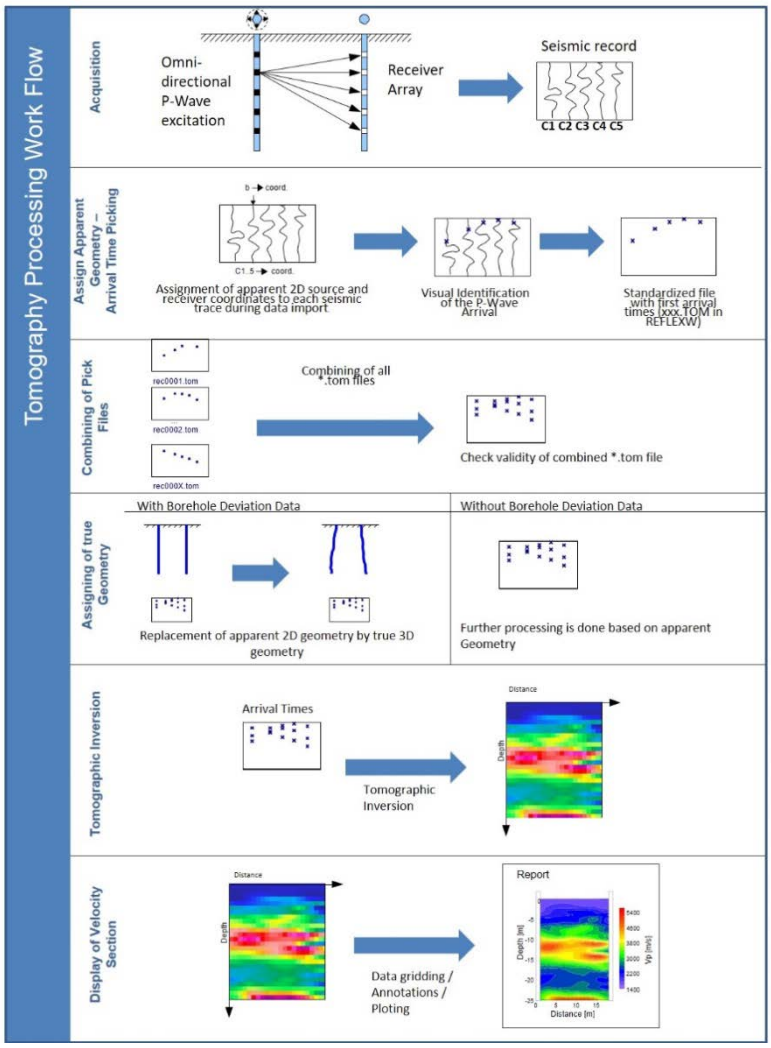


*Figure 3. Workflow for conventional tomographic inversion*

The tomographic inversion can be done with several programs, such as GeotomCG or ReflexW. After converting to the correct input format, the inversion program usually requires a starting model containing seismic velocities next to the traveltimes with the relevant geometry and the number of grid points. Before starting the inversion,

the user has to set the iteration and velocity limits relevant to the dataset and can then start the inversion. Sometimes it is required to use a separate software which includes data gridding, annotations and plotting to display the velocity section.

## 1.3 Uncertainties

The assessment of the uncertainty in the data is complex and site-specific and, therefore, a difficult task. The benefit of crosswell measurements depends on the existing velocity contrasts in the subsurface. Uncertainty is related to field environment (e.g. noise sources such as traffic or other industrial sources), field setup (e.g. borehole distance, proper borehole installation), data acquisition (e.g. proper coupling, Signal/Noise ratio), data processing ( e.g. error in picking arrival times) and data interpretation.

For the crosswell tomography inversion, the unknown region between the boreholes is discretized into "n" pixels to provide a tomographic image of the generated spatial distribution of wave velocity. It is clear that higher resolution (smaller seismic source positions) implies smaller pixel size and, therefore, a higher number of unknowns which turn out to be a bad-conditioned problem. It shows that the smaller the number of receivers accessible for certain signal source positions, the more ill-conditioned the problem is. Likewise, the wavelength used determines the maximum achievable resolution. Anomalies smaller than the wavelength are not resolvable. As already mentioned, there must always be a velocity contrast between the anomalies and the surrounding medium.

Boundary conditions such as borehole casing and the relative impedance between casing-soil affect the radiation patterns and the adequate size of the source. Material losses cause additional attenuation, and the amplitude of the signal receiver must be greater than the noise amplitude. Appropriately filtering or stacking can achieve a higher Signal-to-Noise ratio at the receiver. The sampling theorem shows that the smallest possible wavelength must be at least twice the distance between the recorded positions to give good results.

It is well known that the data quality of seismic signals varies greatly, not only from region to region but even inside one dataset. The data quality can vary from excellent to very low. It is evident that in the case of excellent data quality, the first arrival time picking is easier and more accurate than picking seismic signals, which are contaminated by much noise. Generally, the data quality of seismic signals is not considered in the tomographic inversion. The present tomography inversion scheme mixes traveltimes of seismic signals with low and excellent data quality but treats them equally weighted within the inversion, but the signal-to-noise ratio influences the accuracy of a traveltime pick. Thus, the larger the noise, the lower the reliability of a traveltime pick. If the related uncertainty is not addressed within a tomographic inversion process, all picked traveltimes have the same weight and contribute equally to determining the seismic velocities within a seismic tomogram. In other words, a seismic velocity determined by a “perfect” traveltime pick competes with an uncertain velocity estimate of a poor traveltime pick.

## 1.4 Seismic tomographic inversion using data quality and residual error maps

The quality of the seismic data significantly influences the accuracy of the arrival time picking but is generally not considered in the inversion. Therefore, an evaluation of the signal-to-noise ratio of the data should be carried out.

The signal-to-noise ratio is calculated by the ratio of the maximum first arrival amplitude and the average noise amplitude before the first arrival, and a quality factor (QF) is determined (see Figure 4).

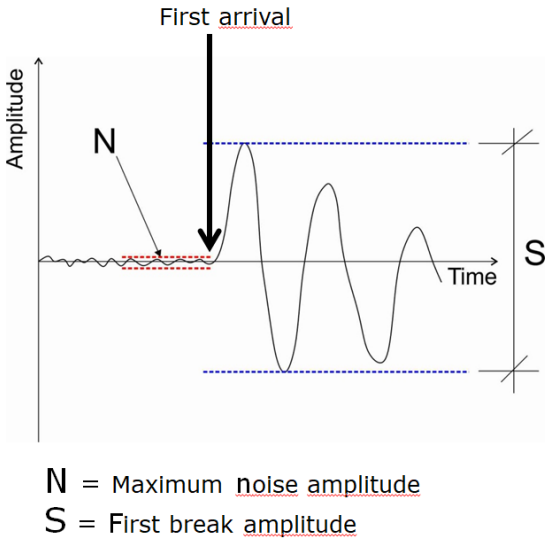


*Figure 4. Determination of the Signal-to-Noise ratio*

A study was carried out by Mackens et al. (2014) which indicates that the improvement in accuracy of picking times tends to level off as the signal-to-noise ratio continues to improve, so the QF values assigned to represent data quality should reach a maximum at some threshold instead of continuing to increase with increasing signal-to-noise ratio.

To account for the traveltime picking error, a data quality-dependent weighting into the well-known SIRT tomography inversion procedure can be introduced. Within this procedure, a QF value to each seismic ray "k" calculated from the signal-to-noise ratio of the seismic trace is assigned. The QF value (normalized signal-to-noise ratio) can be implemented in the SIRT slowness correction scheme [Mackens et al. 2014, Fechner et al. 2015]:

$$\Delta s_n = \frac{1}{\sum_k QF_k} \cdot \sum_k \frac{QF_k \cdot \Delta t_k \cdot r_{n,k}}{\sum_m r_{m,k}^2} \qquad \text{eq. 1}$$

with

- $\Delta t_k$ → traveltime residual of ray "k"
- $r_{n,k}$ → length of raypath segment (ray "k") in voxel "n"
- m → index of raypath segments belonging to ray "k"
- $QF_k$ → quality factor of ray "k"
- $\Delta s_n$ → slowness residual in voxel "n"

If all QF values are equal, equation 1 reduces to the well-known SIRT slowness correction procedure. Implementing the QF value in the inversion procedure automatically assigns a higher weight to rays with higher QF value and less to rays with low QF. Consequently, seismic velocities of rays with higher QF will have a greater contribution to the cell's velocity than those with lower QF, i.e., the averaged velocity comes closer to the seismic velocity of

higher weighted rays. After the final iteration, the distribution of the average QF value in each cell or voxel can be plotted next to the seismic velocity distribution. The QF value distribution shows areas with low and high QF values, thus with lower or higher reliability of the seismic velocity. In this way, the QF value distribution supports the interpretation and evaluation of a seismic tomogram. The procedure has been implemented in GeoTom software.

# 2 DAS Data Interpretation

## 2.1 Introduction to Distributed Acoustic Sensing (DAS)

DAS is a relatively new and rapidly developing technology, and it provides a novel tool for seismic imaging because it is sensitive to local axial strain changes or strain rates along the fibre. The technology provides the simultaneous acquisition of thousands of sensing channels using just one standard optical fibre as the sensing element [Parker et al. 2014]. A DAS interrogator measures Rayleigh's backscattered light of the laser pulse due to imperfections in the fibre. It is a distributed measurement, and the interrogator measures the optical phase of signals returning from the same gauge over two repeated laser pulses between consecutive gauges (over a gauge length, LG). This produces a strain-rate measurement. Gauge lengths are conventionally a few metres to tens of metres [Dean et al. 2017] . Since the boreholes used in this data acquisition are only ~100m deep and the measurements are high frequency, a short gauge length interrogator of 3m is chosen.

Some advantages of DAS data include high spatial (~m) and temporal resolution (~ kHz) measurements; continuous, real-time measurements along the entire length of a fibre optic cable up to >100 km; and relatively time-efficient and low-cost monitoring. However, the recording is a 1-component (1C) measurement because DAS is only sensitive to changes axial to the fibre. DAS has a $\cos^2$ dependence response to P-waves, where $\theta$ is the incidence angle measured from the fibre axial direction [Willis et al. 2016b] and therefore has a reduced response to P-waves arriving close to broadside to the cable, as is the case in crosswell measurements for sources and receivers at similar depths. To mitigate this effect, helically wound cables (HWC) with fibres wound around the cable core have been developed [Kuvshinov, 2016], although the number of deployments is limited. The Svelvik site offers the opportunity to compare data collected on a linear and a HWC to investigate their application to crosswell measurements.

DAS technology is often used to collect Vertical Seismic Profile (VSP) data in oil and gas exploration and has successfully been applied to image CO2 plumes at CCS sites [Daley et al. 206, Hallday et al. 2018, Yurikov et al. 2022]. However, to date, crosswell applications of this technology have not been reported, although modelling design studies have been conducted [Wuestefeld and Weinzier, 2020].

## 2.2 Characteristics of DAS measurements

Figure 4 shows an example of the Linear fibre DAS recording after a 100 – 1700 Hz band pass filter, for a P-wave source at 50 m depth. It presents a direct P-wave from 0.012 s (near source) to 0.03 s (far from source). Since the distance of the well is 20 m, we can roughly estimate P velocity to be ~1700 m/s. Comparing Figures 1 a and b, we can see that the HWC channels are slightly noiser, although noise level changes over each channel, which might be due to a less well-coupled HWC. Additionally, HWC channels have a lower P-wave signal at depths far from the

source, while Linear fibre has lower P-wave signal at near-source depth, which is expected from the sensitivity of HWC and Linear cables.

Although a P-wave source, we see that an S-wave is also generated, the arrival of the S-wave at 0.06 s indicates an S velocity ~ 300 m/s. S-wave amplitude shows substantial variation over depth, which could partly due to the directional DAS strain measurement, but the high amplitude zones around 70 m and from 90 to 100 m, might be due to amplification. Large S-wave amplitude is observed on Linear cable compared with HWC, which suggest S-wave particle motion to be dominantly along the vertical direction, and thus dominantly SV.

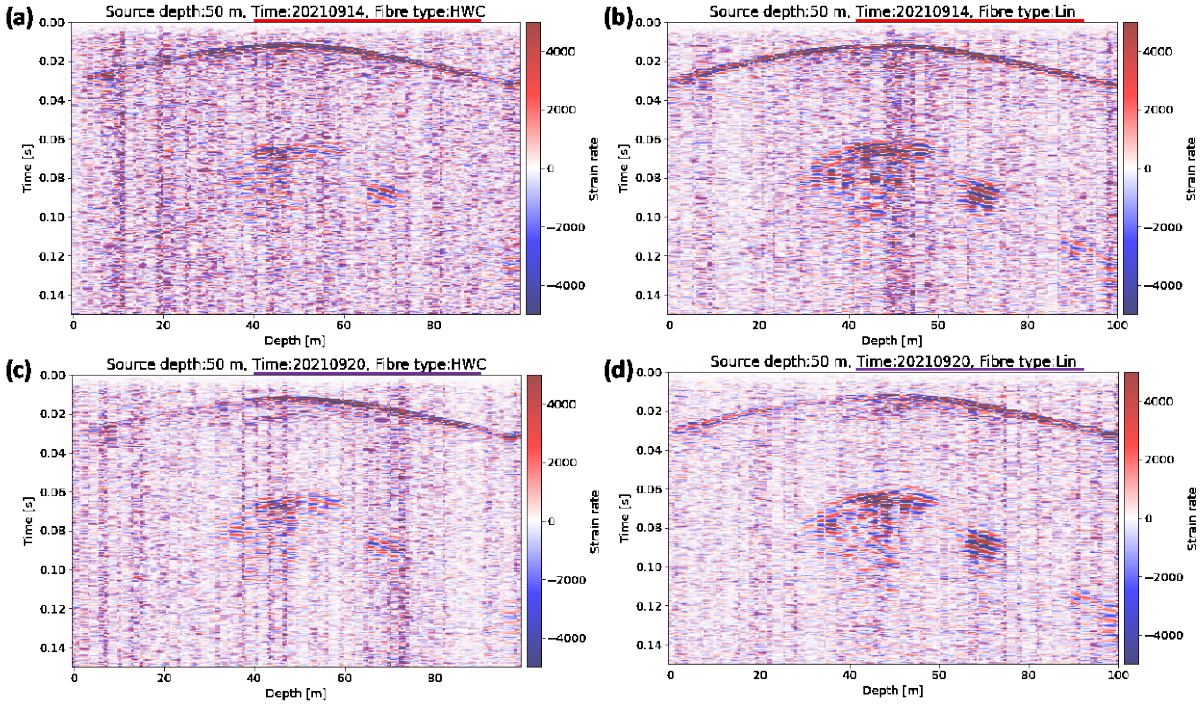


*Figure 5. Stacked shot gathers for source at 50 m depth. (a) HWC recordings from the baseline survey. (b) Linear fibre recordings from the baseline survey. (c) Time-lapse survey after 4 days of $CO_2$ injection, HWC. (d) same as (c) for linear fibre.*

## 2.3 Processing steps for (traveltime) tomographic inversion

*Figure 6. Workflow for DAS tomographic inversion*

## 2.4 Special features for picking first arrivals

As shown in Figure 1, the DAS shot gathers contain intense noise, making it challenging to automatically pick the first arrivals for each DAS channel. We develop a workflow to pick P-wave onset from noiser DAS data, as shown in Figure 7.

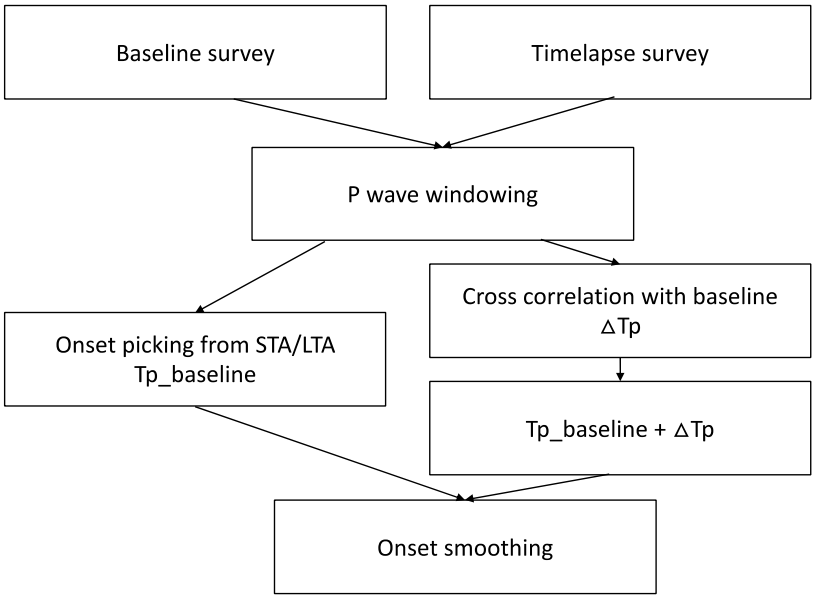


*Figure 7 Working flow for automatic P-wave onset picking*

To reduce false picking, a gaussian window is tapered around a theoretical travel time calculated with an average velocity 1600 m/s (dashed line in Figure). A STA/LTA procedure was applied on each tapered channel, providing independent picks (solid black curves in Figure). The picks on each channel are fluctuated due to strong noise and step features due to a gauge length effect. A Savitzky-Golay filter (smoothing) is applied with a window length of 21 samples (~10.5 m), which produces a smooth first arrival curve (green curves in Figure).

From 8 a and b, we can see that HWC pickings are stable around source depth, while Linear cable pickings are more stable at large offsets.

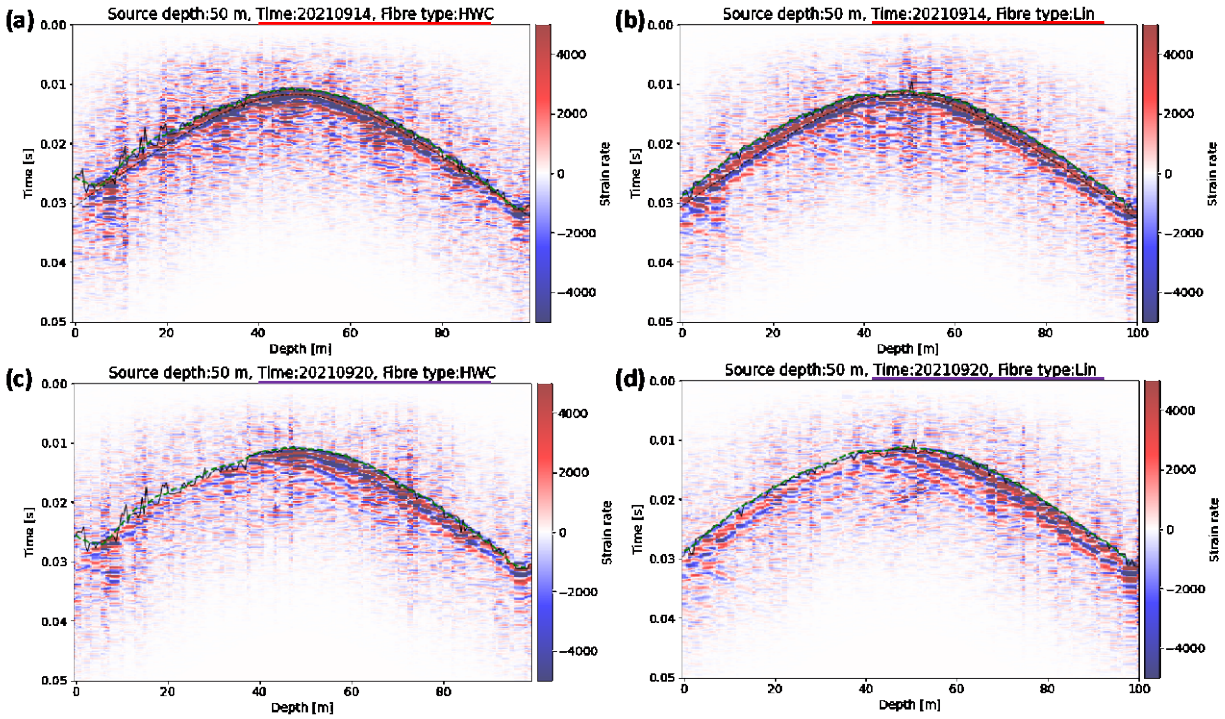


*Figure 8. P-wave first arrival picking from a Gaussian tapered DAS data.*

Due to $CO_2$ injection, the direct P-wave signals damp significantly, especially at a depth of around 30 m (Figure 7 c, d). Direct picking from the time-lapse survey is thus even more challenging compared with the baseline survey. However, since the time-lapse survey has sources at repeated depths as the baseline, cross-correlations can be calculated between the two surveys, and a relative traveltime can be obtained from the delay time of maximal cross-correlations.

Since cross-correlations provide higher accuracy of relative traveltime measurements, we expect the timelapse changes resolved from the tomography inversions to be more reliable than the baseline image due to the higher noise level and aliasing induced by gauge length on DAS.

## 2.5 Limitations and specifics

As stated before also data quality of DAS seismic signals varies greatly. First, the correctness of automatic picking routines also influences the data quality. In conventional seismic data processing, automatic picking routines such as MER, STA/LTA or slope ratio methods provide some indication, but their correctness and uncertainty depend on the seismic data quality. If the data quality is bad, such algorithms do not provide reliable picking results. Filtering can improve that data quality to some extent. However, manually repicking or generally manually picking by experienced persons is always required for reliable, consistent results.

# 3 Field Experiment

## 3.1 Field site

The Svelvik $CO_2$ Field Lab is a unique field laboratory for monitoring experiments that fills the gap between bench laboratory experiments and pilot-scale studies [Eliasson et al. 2019]. It is located at the Svelvik ridge about 50 km southwest of Oslo at the outlet of the Drammensfjord. The ridge is formed by glaciofluvial-glaciomarine terminal deposits formed during the Ski stage of the Holocene deglaciation [Sørensen, 1981; Melø,2011]. Bedrock can be found between 300 and 400 m below the surface. In the central part of the ridge with the top 70m above sea level, sand has been excavated since 1915. Clay layers onlap both flanks of the ridge below sea level. To the south, the thick clay/silt layer fills the bedrock basin up to a few meters below sea level, while to the north, the thinner clay/silt layer is at water depths of 100 - 120 m [Bakk et al. 2012].

## 3.2 Data acquisition and monitoring setup

The Svelvik $CO_2$ Field Lab consists of a central injection well (B2), four monitoring wells (M1-M4) and the necessary infrastructure to carry out $CO_2$ injection experiments (see figure 1). The injection well is designed to inject $CO_2$ under small overpressure conditions and is screened between 64 to 65 m depth. The four monitoring wells are cased with PVC casing to approximately 100 m deep and positioned at the corners of a rhombus around the injection well. The monitoring wells are located at 9.9 m (M3 and M4) and 16.5 m (M1 and M2) from the injection well. Boreholes M1-M2 are oriented in the East-West direction, while the boreholes M3-M4 are oriented North-South.

Fibre-optic cables are installed in each of the monitoring wells. These include a cable containing a linear multi-mode fibre (used for DTS measurements) and cables with a linear and a helically-wound (HWC) single-mode fibre (used for DAS measurements). The linear and HWC fibres are spliced to form one loop for DAS interrogation, as shown in Fig. 2. The fibre-optic cables are clamped to the outside of the casing of each borehole. Layers of cement and gravel fill the annulus.

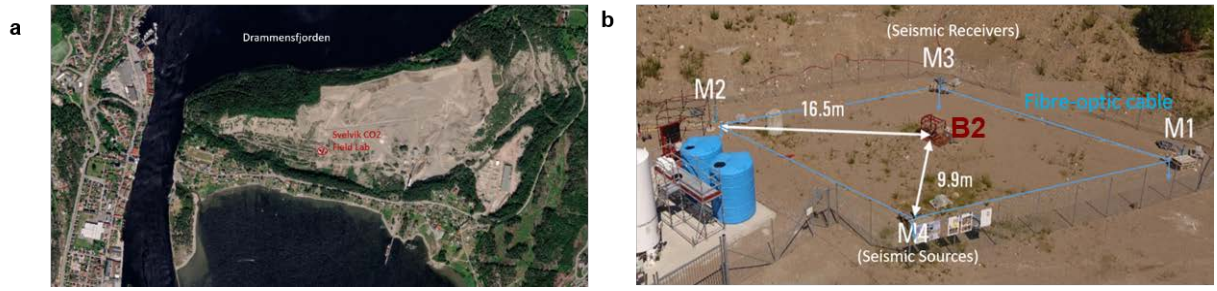


*Figure 9 (a) Location of Svelvik $CO_2$ Field Lab (Source: Bing Areal); (b) Svelvik $CO_2$ Field Lab with injection (centre, B2) and monitoring wells (M1-M4)*

The seismic experiment was conducted from 14 to 22 September 2021, with a $CO_2$ injection starting on 16 September and ending on 22 September. The injection start-up day is referred to as "Day 0", and 21 September is referred to as "Day 5". During the experiment, $CO_2$ was injected at borehole B2 with a daily rate of 8 $m^3$ and a small overpressure of 0.1 bar at the screened casing between 64-65 m over the 6 days. Overpressure was initially adjusted to become stable and subsequently, the active seismic acquisition began.

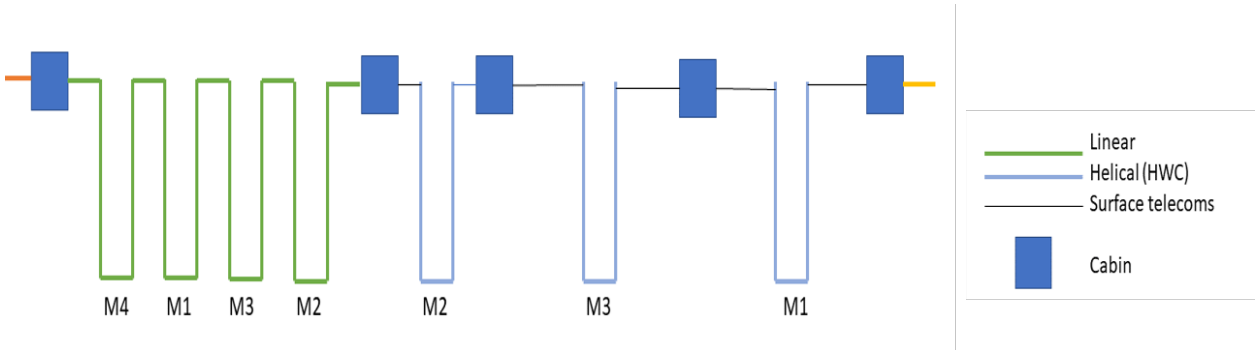


*Figure 10. DAS fibre-optic cable loop used in data acquisition. Boreholes are labelled (M1-M4), and the type of cable (linear, helical or standard telecommunications) is indicated. The cables are spliced together to form one interrogation loop. The interrogator is housed in the cabin.*

For all experiments, the seismic sources were placed in borehole M4 and the hydrophone/geophone seismic receivers in borehole M3. The seismograph recording frequency is 32 kHz for the geophones/hydrophones. DAS data were recorded in all monitoring boreholes with a sampling frequency of 16 kHz. DTS data were also recorded in all four monitoring boreholes. The P-wave source was fired at a 1 m interval between 30 to 77 m depth. Depth refers to the top casing. Two hydrophone strings, each with 24 channels and 1 m sensor separation, were placed in borehole M3, covering the same depth. The S-wave measurements focused on two depth zones, i.e. between 58 m to 72 m and from 32 m to 46 m. The lower zone covered the injection depth and was of interest at the beginning of the injection experiment. The upper zone became of interest at later stages of the experiment as it was known from previous experiments that the clay layer trapped CO2 at about 35 m depth.

One P-, SH- and SV-wave survey was carried out before injection as a baseline measure (see Figure 11). A total of eight P-wave tomography data sets were acquired during the injection. On Day 0 and Day 1, two P-wave surveys were carried out, i.e. one in the morning and one in the afternoon. In the lower zone, SH- and SV-wave surveys were carried out on Days 0 – 2. SH-wave surveys were carried out in the upper zone from Day 1 to Day 5. Unfortunately, the SV-source malfunctioned on Day 1 and could not be used for later surveying. During all the conventional surveys, simultaneous recording by the DAS system was made. The borehole deviation was measured and taken into account during data processing.

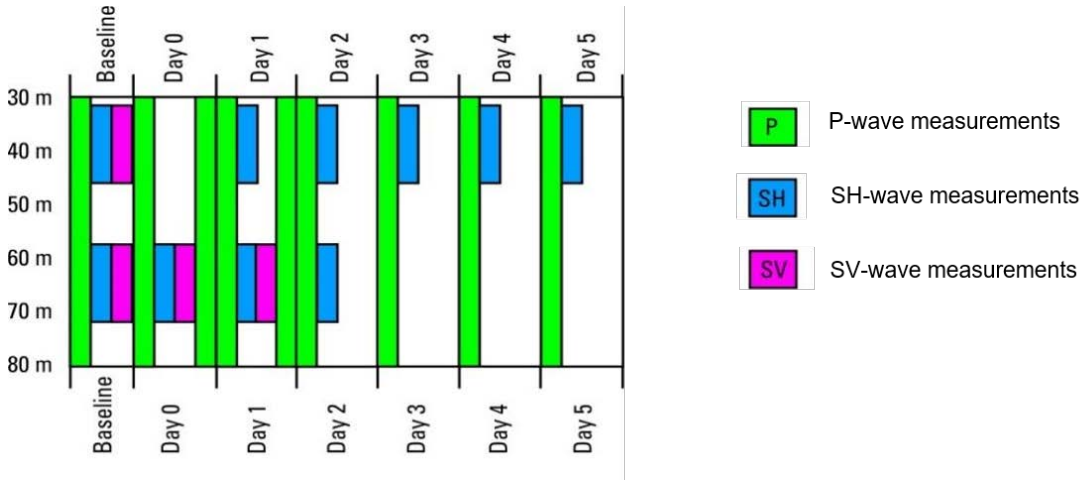


*Figure 11. Seismic field measurement setup showing source positions.*

A Silixa iDAS v2 interrogator was used for DAS data collection. A gauge length of 3 m was used with a channel spacing of 0.5 m. The complete measurement length for the DAS data was 1950 m, including recordings on the linear and HWC fibres. The unit was operated in triggered mode, and data were GPS timestamped. A Sensornet Oryx+ unit was used for the DTS data collection.

# 4 Data analysis and results of Svelvik field data

## 4.1 Conventional data

A first analysis was made using a crosswell data set for each wave type. Thus, only source-receiver pairs with equal depths were considered. Arrival times for all wave types (P, SH and SV) were picked for each crosswell set and seismic velocities were calculated based on true source and receiver distances. Figure 12 shows the calculated P-, SH- and SV-wave velocities for all surveys with depth and the calculated traveltime changes normalized to the baseline survey.

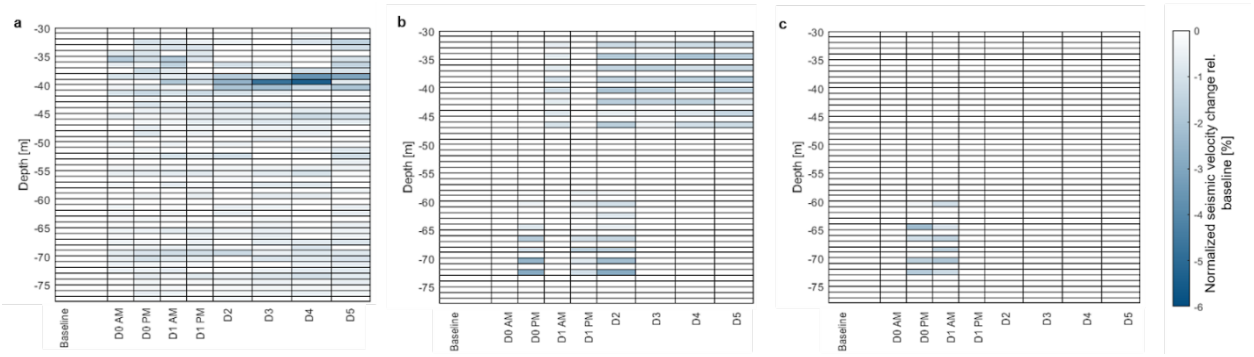


*Figure 12. Cross-well data analysis: temporal changes of the normalized wave velocity in relation to baseline in percentage for (a) P-Wave, (b) SH-Wave and (c) SV-wave*

The temporal changes displayed in Figure 11a show the influence of $CO_2$ gas. Changes are visible shortly after injection starts on Day 0 at different depths. No, or only minor, changes are visible at the injection zone at about 64 m. Significant changes start at Day 2 and Day 3 at a depth of about 38 to 40 m. This corresponds to a drop in seismic velocity from about 2180 m/s to 2140 m/s. Figure 11b and c show a drop in velocity calculated for the SH- and SV-wave velocity for the lower zone around the injection point.

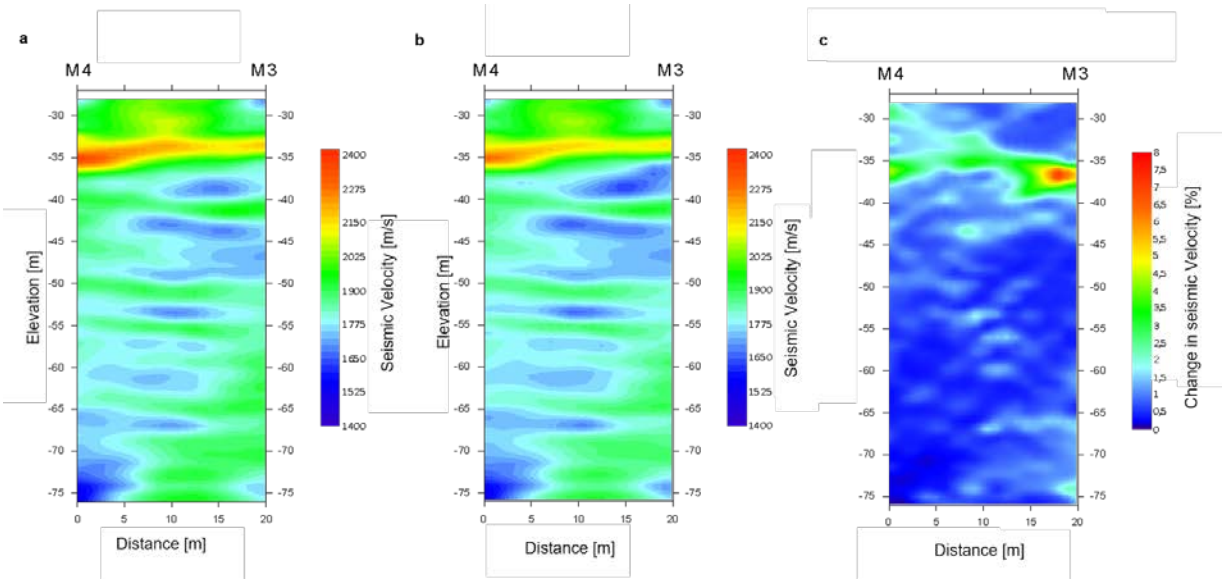


*Figure 13. Tomographic inversion results for (a) P-wave for baseline and (b) Day 4 data. (c ) The difference plot (baseline-Day4/baseline) is shown on the right tomogram.*

Seismic tomography processing was carried out for the baseline survey and data was obtained on Day 4. These data show significant changes, especially at a layer between 35 m and 40 m. Traveltimes were picked on the Day 4 data assuming that traveltimes can only be slower, i.e., all changes occurring during $CO_2$ injection could only lead to a drop in seismic velocity and not an increase of seismic velocity. Furthermore, traveltime data have been limited to a ray angle of +/- 45 degrees to avoid rays with longer paths tending to travel outside the imaging plane. The software GeoTomCG was used to invert the data and calculate the seismic tomograms. The final tomographic model obtained from the baseline data was used as a starting model for the inversion of the seismic data from Day 4. The inversion software comes with a specific inversion option allowing only negative velocity changes during inversion, i.e. velocities can only be smaller or equal to the starting velocities. This is a consequence of the mentioned procedure for traveltime picking. The difference between the two tomograms showing the changes during the time was calculated using the seismic velocity ratio, as displayed in Figure 12. Small changes in velocity up to 7% are visible in the difference tomogram. Changes are predominantly visible right below the high-velocity zone at 35 m. This zone is related to a thick clay layer, most likely acting as a $CO_2$ trap. Minimal changes of less than 2% are visible below 40 m depth.

## 4.2 Distributed Acoustic Sensing (DAS)

As for the conventional seismic data, arrival times for P, SH and SV were picked from DAS stacked waveforms for each crosswell dataset and subsequently, seismic velocities were calculated based on source-receiver distances. Initially, a spectral analysis was performed to determine the signal frequency bandpass, and an appropriate bandpass filter was applied. Bandpass filters of 700-1700 Hz, 50-500 Hz and 100-220 Hz were used for P-, SH- and SV-waves, respectively. An automatic picking algorithm was applied to the P-wave data with manual inspection of the picks. Manual picking was performed on the SH and SV data because the data's signal-to-noise ratio (SNR) is lower.

To assess the suitability of linear and HWC for P- and S-wave surveys, the data are compared using arrival SNR values. For P-wave surveys, theory suggests that linear fibre should have no sensitivity to waves arriving broadside to the cable at exactly 90° incidence. We, therefore would expect low SNR on the linear cable where the source and

receiver are at approximately the same depth. In contrast, the HWC is expected to provide improved sensitivity at near-broadside angles with some sensitivity at all incidence angles. The linear cable is expected to provide the best sensitivity to P-waves arriving near to in line with the cable. Indeed this is what is observed in the data (Figure 14).

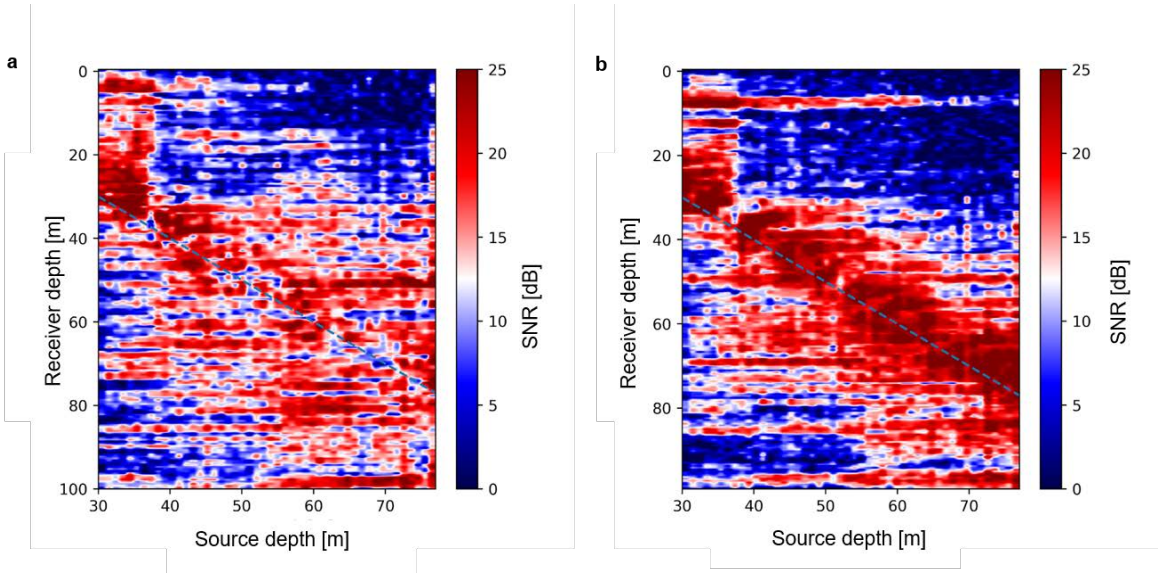


*Figure 14. Comparison of SNR of P-arrivals (a) on the linear fibre and (b) HWC fibre. The dashed line shows equal source and receiver depth where broadside arrivals are expected.*

For S-wave surveys it is expected that the linear fibre will perform better overall than the HWC. The SNR observed in the S-wave surveys is lower than for the P-wave, particularly for the SH survey with a lower power source. However, there is not a significant difference between the performance of the linear and HWC in the S-wave surveys (e.g., Figure 15). Further work is required to assess DAS data for S-wave surveys.

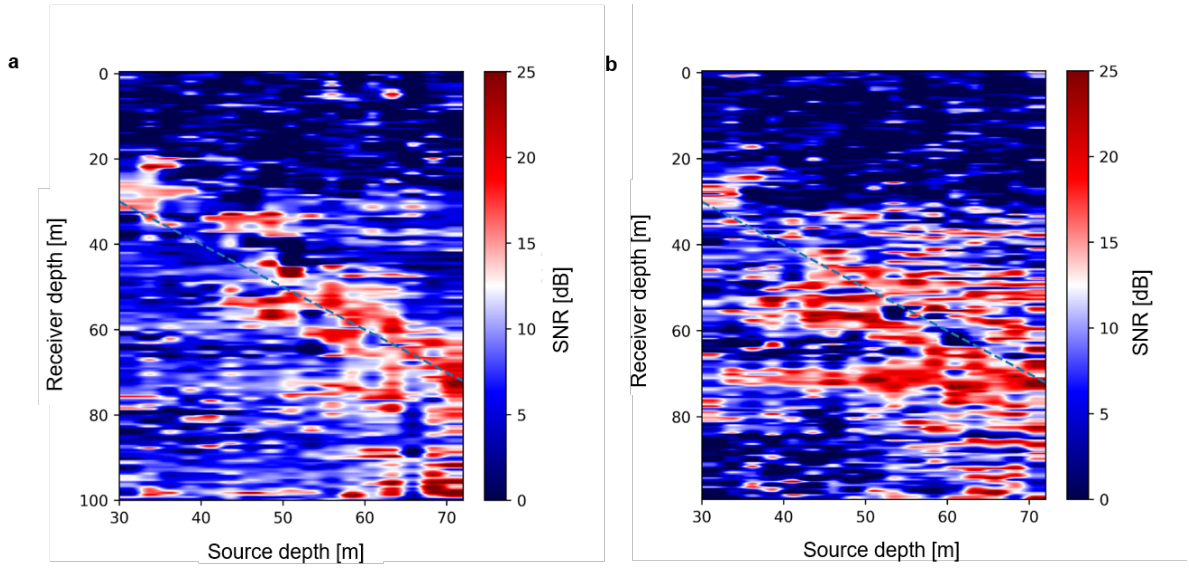


*Figure 15. Comparison of SNR of SV-arrivals (a) on the linear fibre and (b) HWC fibre. The dashed line shows equal source and receiver depth where broadside arrivals are expected.*

In all DAS surveys, apparent differences in signal quality are observed along the length of the fibre, and the regions with a poor signal are consistent between cables and persist in time. This indicates that cables deployed at the site are not optimally and inconsistently coupled to the formation. Thus, neighbouring channels can have high and low SNR. For optimal signal strength, it is advised that cables are cemented in place on the outside of the borehole casing.

P-wave DAS data were subsequently processed using the same tomographic processing method as the conventional data, and a comparison of the baseline results for both linear and HWC data is given in Figure 15. The tomogram derived using the DAS data is similar to the conventional data tomogram, providing confidence in the ability to pick accurate arrival times on the DAS data. In general, the HWC provides higher quality data and combining the HWC and linear datasets (Figure 15c) does not improve the quality. This is due to higher traveltime pick uncertainties due to generally lower SNR in the linear data. There are some differences in the images obtained using DAS (Figure 16) and conventional (Figure 13) data because the DAS data is less well constrained between deep source to shallow receiver ray paths.

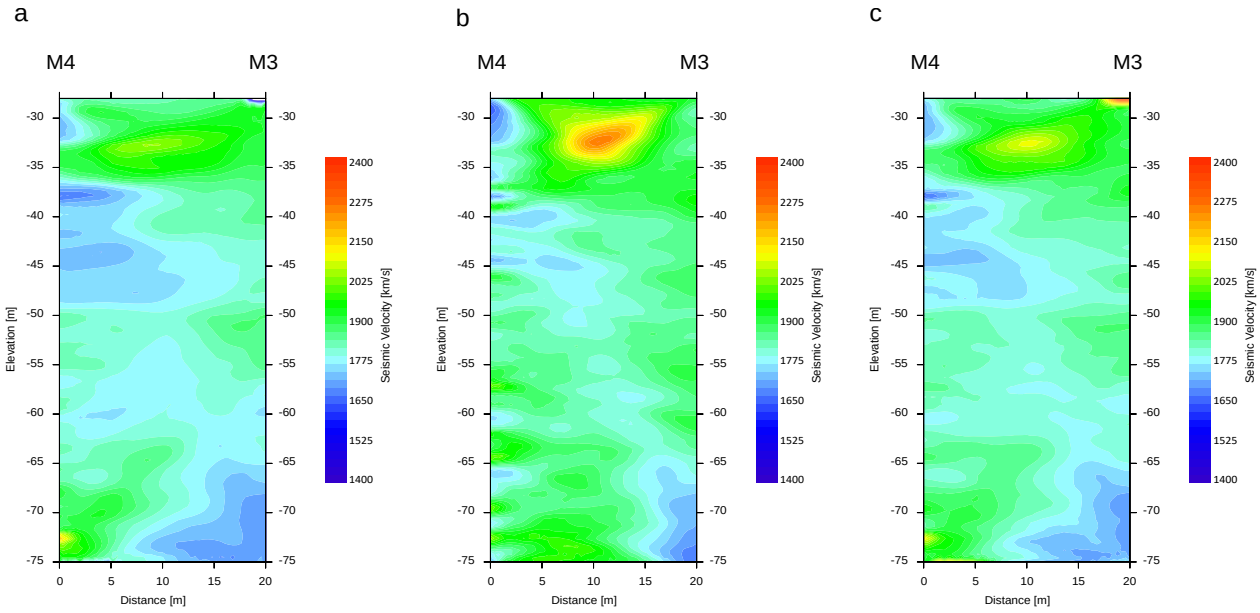


*Figure 16. Tomographic inversion results for baseline P-wave for DAS data recorded on (a) HWC and (b) linear fibres. (c) The panel on the right shows results using all traveltime picks from both HWC and LIN DAS data.*

These results show some inconsistencies and a repicking was done to improve the DAS data quality. The signal-to-noise ratio influences the accuracy of a first arrival time pick, i.e. the more significant the noise, the lower the related reliability of the time pick. Figure 17 shows the normalized SN Ratio of HWC and LIN DAS data in comparison to the conventional seismic data. It can be said that the data quality of the HWC data is better than the LIN data. However, according to that measured DAS data, the quality is not as good as conventional seismic data.

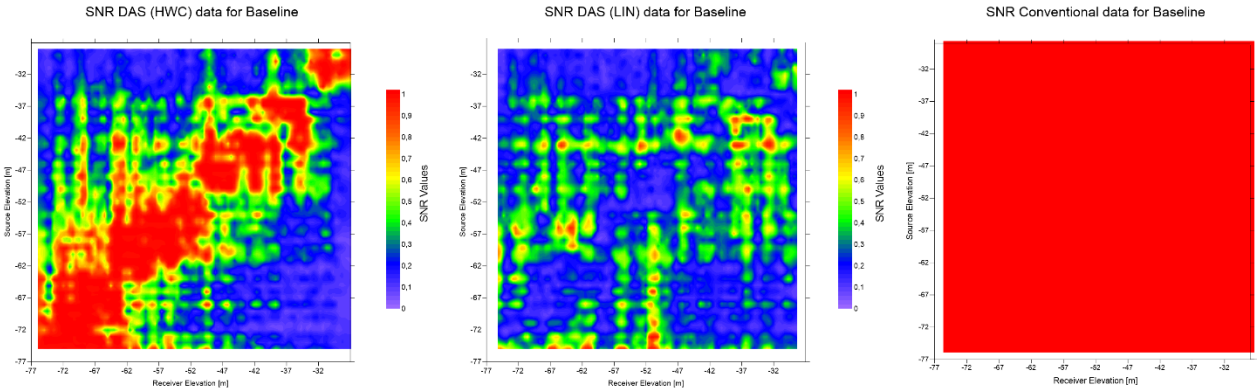


*Figure 17: Normalized SNR Ratio of HWC and Lin DAS data in comparision to conventional seismic data for the baseline measurements with SNR =1 is equal to S/N=10. The S/N ratio for conventional data are generally >=10.*

The normalized residual after 12 Iterations versus ray angle was checked to evaluate the picking quality of the DAS data. Usually, residuals should show a not distinct pattern, i.e. should be equally distributed (like a scatter around "0"). It is visible on the HWC data but not on the LIN data. An angular dependency on the LIN data points to an anisotropy or, rather, a general mispicking due to poor data quality.

(a) Baseline HWC Data (repicked)

(b) Baseline LIN Data (repicked)

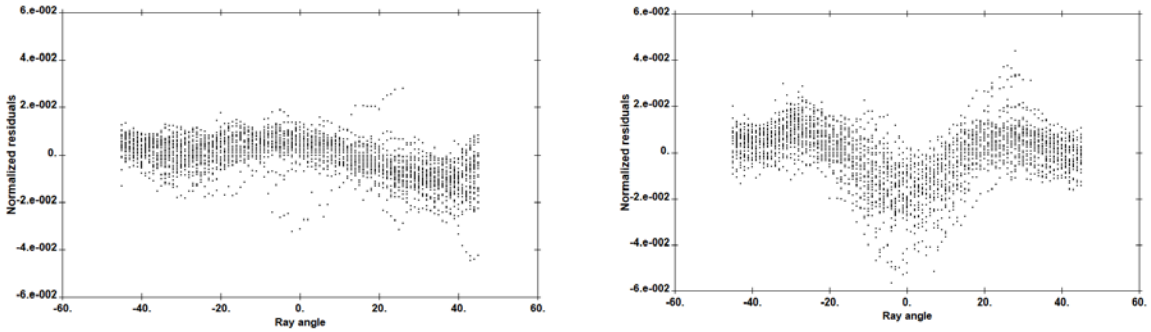


*Figure 17: Normalized residual after 12 Iterations versus ray angle*

Figure 18 shows the slowness residual Δs normalized by the slowness s of a cell. Areas with relative slowness residual errors close to 0 indicate good estimates of the local seismic velocity. Negative or positive relative slowness residual errors are a sign of underestimated or overestimated velocities, respectively. For the repicked baseline HWC data, there is an area between -58 to -77 m where the velocity is underestimated, while for the Baseline LIN data in a depth range from -28 to -40 m there are clear areas with overestimated velocity values. This slowness residual map indicates a non-perfect travel time fit between measured and calculated travel times.

(a) Baseline HWC Data (repicked)

(b) Baseline LIN Data (repicked)

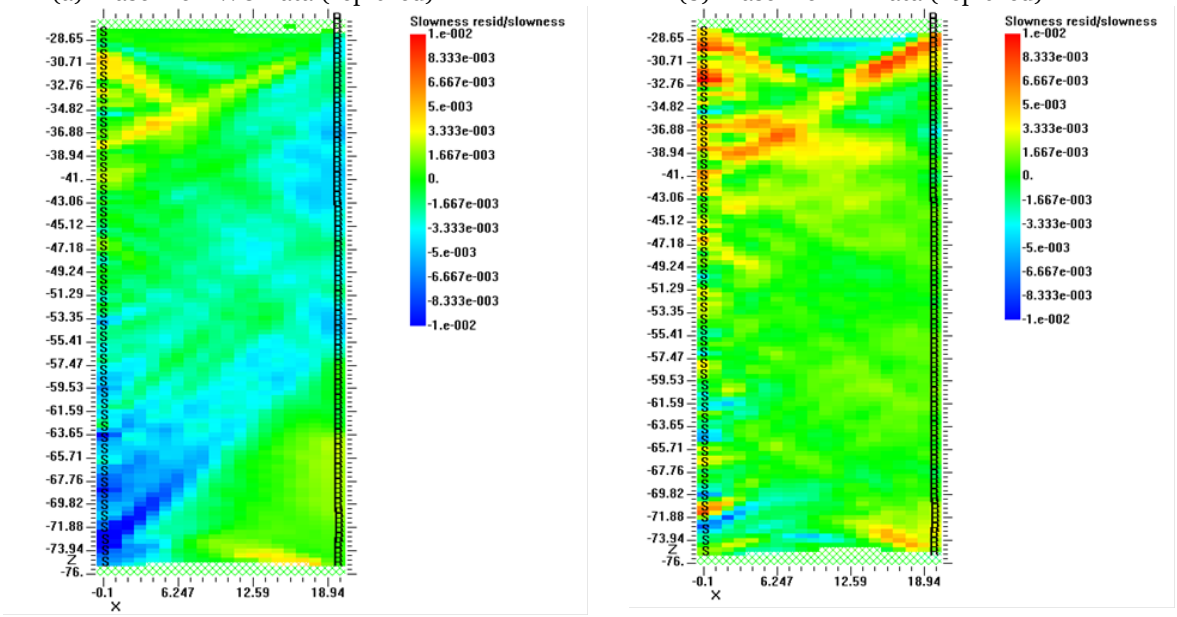


*Figure 18: Slowness Residual after 12 Iterations (positive value = overestimated velocity, negative values = underestimated velocity)*

Figure 19 shows the map of the data quality obtained after 12 Iterations of the same data set introducing quality factors. This map is called the reliability map and shows the average data quality factors distribution for each tomogram cell. Areas with low-quality values are generally where the velocity determination is less reliable, whereas higher quality values point to a more reliable velocity estimate.

(a) Baseline HWC Data (repicked)

(b) Baseline LIN Data (repicked)

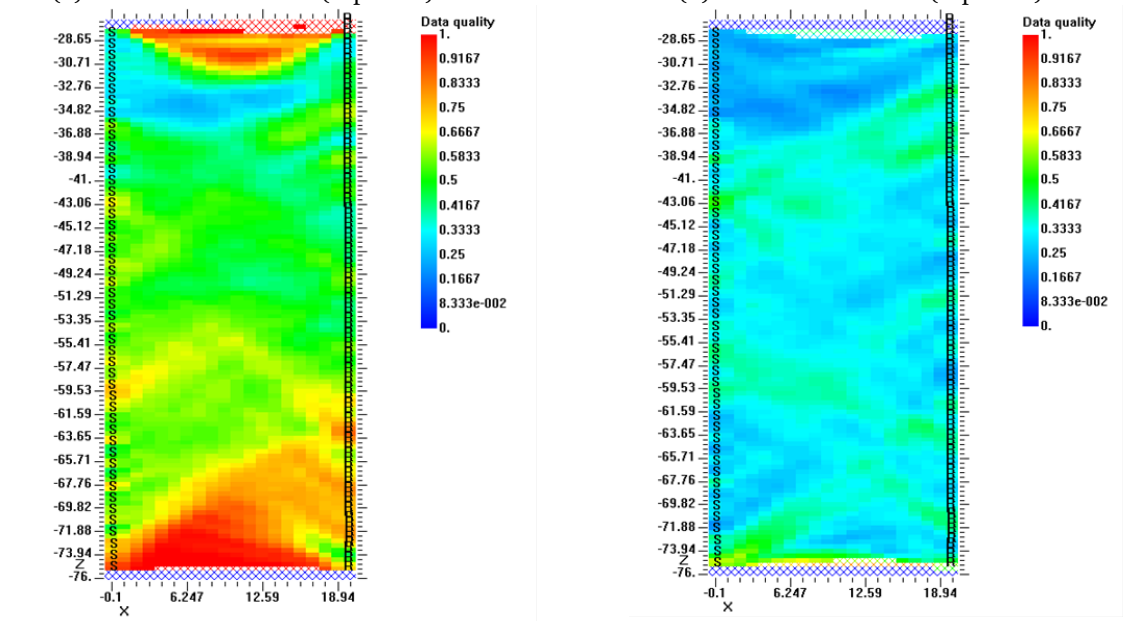


*Figure 19: Data Quality Value after 12 Iterations*

Data quality values close to one can be related to the excellent reliability of the seismic velocity estimation, whereas low data quality values are associated with a poor velocity estimate. The reliability map presented in figure 19 generally shows higher quality factors for the HWC DAS data with an area of low data quality between a depth of -31 to -37m.

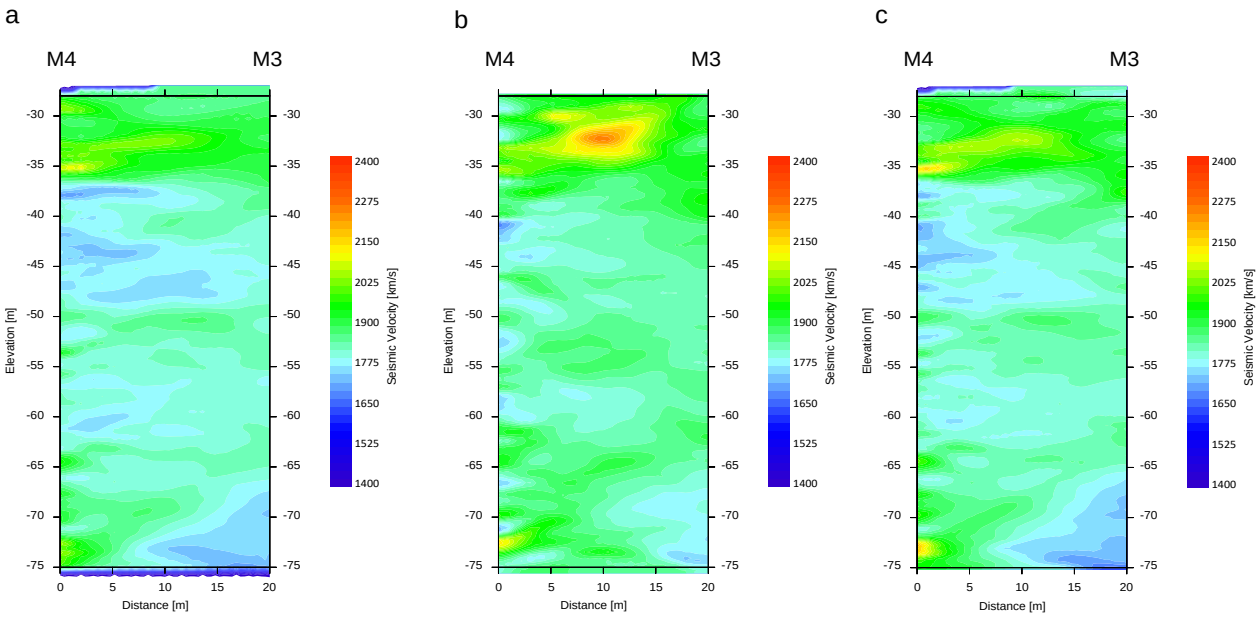


*Figure 20. Tomographic inversion results for baseline P-wave for DAS data repicked on (a) HWC and (b) linear fibres. (c) The panel on the right shows results using all traveltime picks from both HWC and LIN DAS data.*

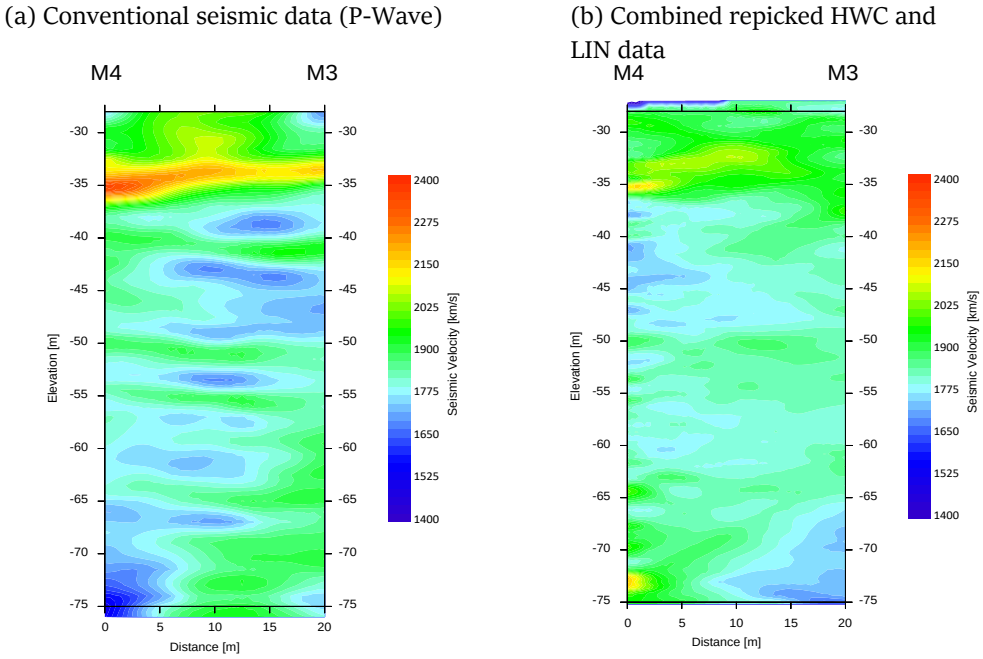


*Figure 21. Comparison of tomographic inversion results for baseline P-wave for (a) conventional seismic P-wave, (b) for repicked traveltime picks from both HWC and LIN DAS data*

The tomographic inversion result of this repicked data is displayed in Figure 20. It can be recognized that the reliability increases compared to Figure 15. However, a difference between HWC and LIN can still be seen. The inversion of all repicked traveltime picks from both HWC and LIN DAS data increase the interpretability of the DAS data. Comparing all tomographic inversion results shows that the conventional and repicked DAS data are comparable.

# 5 Conclusion

The tomographic inversion procedure was applied to conventional, HWC and LIN DAS data. Data quality was calculated based on the signal-to-noise ratio of the seismic data. The tomographic inversion software GeoTomCG was applied to allow that quality factors calculated from signal-to-noise ratios to be part of the input data. It was recognized that the quality of the seismic data significantly influences the accuracy of the arrival time picking.

The data quality of the DAS data was generally lower compared to the quality of the conventional seismic data. Also, the application of state-of-the-art automatic picking routines for first arrival picking of the DAS data indicates some restrictions due to reduced data quality. Generally, the data quality of HWC data is higher compared to the LIN DAS data, even after filtering.

A manually repicking of the DAS data improved the data quality and, therefore, the tomographic inversion results. Hence, the tomographic inversion results of the conventional and the DAS data generally show the same features.

# 6 References


Bakk, A., Girard, J.-F., Lindeberg, E., Aker, E., Wertz,F., Buddensiek, M., Barrio, M., Jones, D. (2012). CO2 Field Lab at Svelvik Ridge: Site Suitability, Energy Procedia, Volume 23, 306-312, Doi: 10.1016/j.egypro.2012.06.055.

Daley, T.M., Miller, D.E., Dodds, K., Cook, P., Freifeld, B.M (2016) Field testing of modular borehole monitoring with simultaneous distributed acoustic sensing and geophone vertical seismic profiles at Citronelle, Alabama. Geophys. Prospect. 64, 1318–1334.

Dean, T., Cuny, T., Hartog, AH. (2017) The effect of gauge length on axially incident P-waves measured using fibre optic distributed vibration sensing. Geophys. Prospect. 65:184–93

Dines, K A, and Lytle, R J. (1979) Computerized geophysical tomography. United States: N. p., Web. doi:10.1109/PROC.1979.11390.

Eliasson, P., Cerasi, P.,Romdhane, A., White, J., Schmidt-Hattenberger, C., Carpentier, S., Grimstad, A-A.,Lothe, A. (2019). Pressure Control and Conformance Management for Safe and Efficient CO2 Storage – An Overview of the Pre-ACT Project. SSRN Electronic Journal. 13. 10.2139/ssrn.3365876.

Fechner, T., Ehosioke, S.I., Mackens, S., Karl,L., ,Tweeton, D. (2015). Reliability maps for seismic tomography, ICEG Conference, 15.-18 November 2015, Al Ain – UAE

Halladay A., V. Orpeza Bacci, S. O'Brien, K. Hindriks (2018) Results from the second monitor DAS VSP at Quest CCS, EAGE Fifth CO2 Geological Storage Workshop, doi: 10.3997/2214-4609.201802981.

Mackens, S., Albers, W.,Fechner, T., Tweeton, D., Karl, L. (2014). Interpretation of seismic tomography results using data quality and residual error maps. 79-84. 10.1190/SAGEEP.27-035.

Melø, T. (2011). Hydrogeology of the shallow aquifer at the Svelvik ridge. 2011: MSc thesis, University of Oslo, Norway

Parker,T.,Shatalin,S.,Farhadiroushan, M. (2014). Distributed Acoustic Sensing – a new tool for seismic applications, first break volume 32, February 2014

Sørensen, R. (1981). Foreløpig beskrivelse til kvartærgeologisk kart SVELVIK – CL 083, M1:10 000. 1981: The Geological Survey of Norway, Report 1807/7.

Willis, M. E., D. Barfoot, A. Ellmauthaler, X. Wu, O. Barrios, C. Erdemir, S. Shaw, and D. Quinn, 2016b, Quantitative quality of distributed acoustic sensing vertical seismic profile data: The Leading Edge, 35, 7, 605–609.

Wuestefeld, A. and W. Weinzier (2020). Design considerations for using Distributed Acoustic Sensing for cross-well seismics: A case study for CO2 storage, Geophysical Prospecting, 68, 1893–1905.

Yurikov A., K. Tertyshnikov, S. Yavuz, P. Shashkin, R. Isaenkov, E. Sidenko, S. Glubokovskikh, P. Barraclough, R. Pevzner (2022) Seismic monitoring of CO2 geosequestration using multi-well 4D DAS VSP: Stage 3 of the CO2CRC Otway project, International Journal of Greenhouse Gas Control, 119, 103726.